Accepted Manuscript

Inverse optical flow based guidance for UAV navigation through urban canyons

Pooja Agrawal, Ashwini Ratnoo, Debasish Ghose
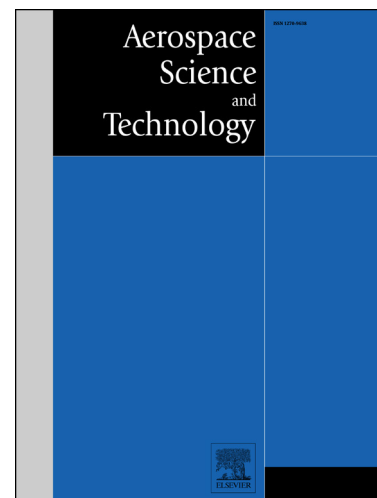
Please cite this article in press as: P. Agrawal et al., Inverse optical flow based guidance for UAV navigation through urban canyons, *Aerosp. Sci. Technol.* (2017), http://dx.doi.org/10.1016/j.ast.2017.05.012

Inverse Optical Flow Based Guidance for UAV Navigation Through Urban Canyons

Pooja Agrawal *, Ashwini Ratnoo †and Debasish Ghose ‡

Indian Institute of Science, Bangalore, 560 012, India

The paper proposes a vision based guidance strategy for an unmanned aerial vehicle (UAV) navigating through urban canyons. The UAV has a single forward facing camera and relies on optical flow computed from the sequence of images captured by the camera. The steering command is inversely proportional to the optical flow difference between the two sides of the image. This leads to high turning and safe motion while directly facing an obstacle or a wall. Analysis is carried out for infinite and finite length obstacles to highlight the obstacle avoidance properties of the proposed strategy as compared to a widely used existing strategy. Realistic simulation studies with straight, L, and T shape canyons and combination of them show the viability of the proposed strategy while navigating through urban canyons.

I.   Introduction

For urban operations such as surveillance, rescue and search, a UAV has to fly at low altitudes in unstructured and unknown environments. In order to perform such operations UAVs should have on-board capability of detecting and avoiding obstacles such as buildings and structures. Infra-red, sonar and laser sensors can be used to detect obstacles. However, these sensors have limitations as laser sensors are heavy in weight, sonar sensors provide slow updates and infra-red sensors are sensitive to external light [1]. Small UAVs have limited payload capability and this motivates the use of light

---

*Research Student, Autonomous Vehicles Laboratory, Department of Aerospace Engineering, Indian Institute of Science, Bangalore, 560 012, India, pooja.iitd@gmail.com

†Assitant Professor, Autonomous Vehicles Laboratory, Department of Aerospace Engineering, Indian Institute of Science, Bangalore, 560 012, India, ratnoo@aero.iisc.ernet.in

‡Professor, Guidance, Control and Decision Systems Laboratory, Department of Aerospace Engineering, Indian Institute of Science, Bangalore, 560 012, India, dghose@aero.iisc.ernet.in.

weight vision sensors. Moreover, vision sensors provide very rich information about the environment.

Many vision based avoidance techniques have been proposed for ground robots [2–6] and aerial vehicles [1, 7–16] navigating in unknown environments. These techniques are mainly based on optical flow [1, 3, 4, 6, 7, 9, 11] or stereo vision [12, 13, 17, 21]. Although both the techniques can detect obstacles, stereo vision is computationally expensive and requires more than one camera.

A common optical flow based guidance strategy tries to keep the vehicle position equidistant between the obstacles by balancing the optical flow on both sides of the vehicle. This strategy is known as center response [22, 23] or balance strategy [1, 3, 7]. Balance strategy is widely used for ground robots [3, 6], helicopters [1] and quadrotor UAVs [7, 9] that use a single camera to navigate through urban environments. By maintaining equal optical flow on both the sides, the balance strategy is effective in scenarios with obstacles on both the sides of the vehicle such as a corridor.

Although balance strategy works well in the corridor scenario, it leads to severe performance deterioration in scenarios where the camera directly faces an obstacle or a wall. Under such scenarios, maintaining an equal optical flow on both the sides will eventually lead to a collision with the obstacle. As most real life environments are complex and are composed of a combination of differently sized and shaped canyons, the probability of facing an obstacle in front of the vehicle is high. For instance, consider an L or T shaped corridor, in which as the vehicle flies to the end of one arm of the corridor, it faces a wall at the point where the corridor turns. Even otherwise, in a simple straight corridor, due to perturbation in the trajectory, the vehicle may get into a situation where it faces one of the corridor walls.

In [3], the problem with the balance strategy is addressed by computing the time-to-contact information to identify scenarios where the vehicle is about to collide with an obstacle situated directly ahead. If the time-to-contact is less than a predefined value, the UAV takes a tight U-turn [1] to avoid crashing into the wall.

The strategy presented in this paper overcomes these limitations of balance strategy for a UAV navigating through urban canyons. The proposed strategy generates a turn rate command which is inversely proportional to the optical flow difference between the right and left side sub-images of the image as obtained from a front facing camera. Hereinafter, the proposed strategy is referred to as inverse strategy. Because of its inverse relation with the optical flow difference, inverse strategy generates a high turn rate command to avoid front obstacles.

In this paper, the 3D environment is created with real texture images, which are captured on 2D image plane using a front facing camera. The captured images are preprocessed to filter out the noise. Next, to get the environment information, the image feature points are extracted from the image. The optical flow vectors are used as image features, computed from a sequence of two consecutive images. Based on the optical

flow information, a guidance law is designed and analyzed for UAV safe motion. Finally, the proposed guidance is validated in realistic simulation environments with high fidelity UAV 6DoF model. The work focus mainly on the theoretical development, analysis, and realistic validation of a new guidance approach. Implementation in actual hardware would be beyond the scope of the paper. Fig. 1 shows the block diagram of the proposed methodology.

Image processing

UAV with camera → Sequence of color images → Color to grayscale conversion → Image down-sampling → Image feature extraction

Guidance strategy ← Optical flow
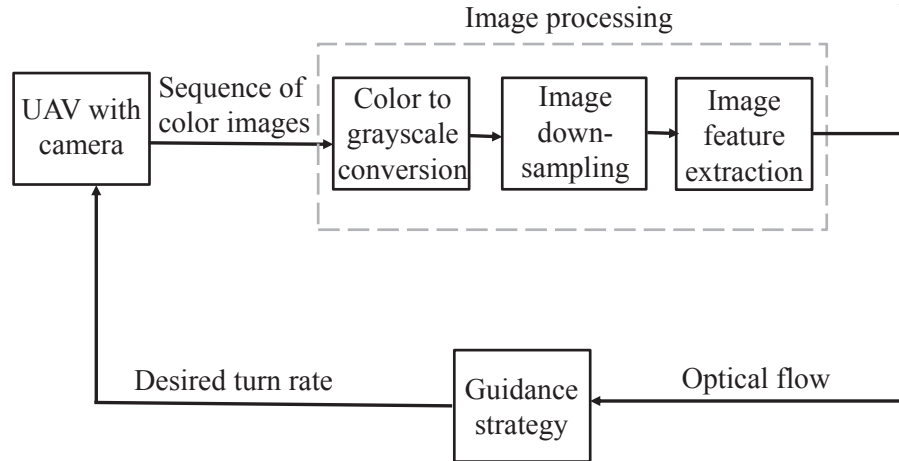
Desired turn rate ← Guidance strategy

Figure 1: Obstacle avoidance block diagram.

The remainder of the paper is organized as follows: Section II describes the problem formulation and models. Optical flow and its estimation using the Horn-Schunk method is discussed in Section III, followed by the guidance strategies in Section IV. Section V presents an analytical comparison of avoidance properties between the guidance strategies. Section VI contains the simulation results and comparisons. Section VII summarizes the results and points to future work.

II.   Problem Formulation and Models

A.   Problem Definition

Consider urban canyon scenarios shown in Fig. 2, where straight, L, and T shaped show the generic scenarios. Fig. 2 (d) shows a specific scenario with an L shaped canyon leads to a T junction. Point S shows the starting position of a UAV is equipped with a forward facing camera that provides optical flow information as computed from the sequence of images. A prospective guidance strategy should be able to navigate the UAV through such canyons without colliding with canyon walls. Further, the strategy should be robust enough to provide safe motion for different UAV initial positions and heading directions.
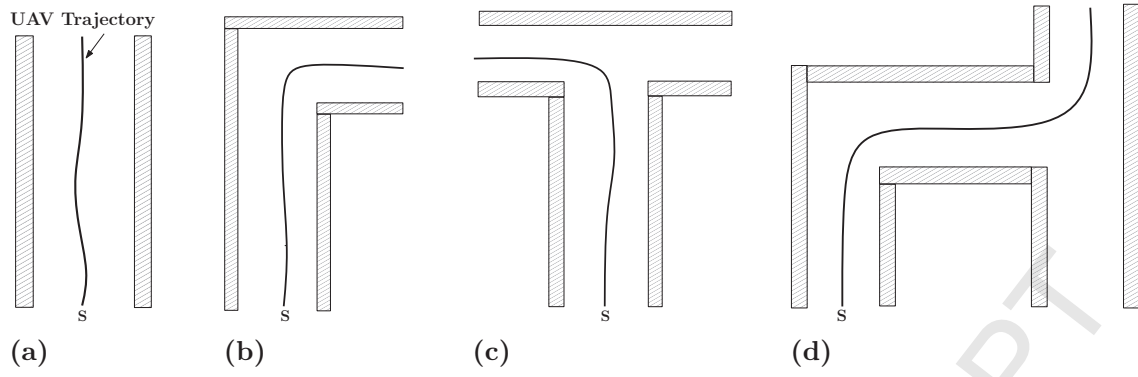
(a)   (b)   (c)   (d)

Figure 2: UAV navigation through urban canyons (a) Straight (b) L shape (c) T shape (d) Combination of L and T shapes.

B. UAV Kinematic Model

The UAV is assumed to be a constant speed point mass moving in a plane as shown in Fig. 3. The equations of motion are given as

$$\dot{x}_a = V \cos \psi \tag{1}$$

$$\dot{y}_a = V \sin \psi \tag{2}$$

where, (x_a, y_a), V and ψ represent the position, speed and heading of the UAV, respectively. The turning rate guidance command is governed by

$$\dot{\psi} = \frac{a_a}{V} \tag{3}$$

where, a_a is the guidance command applied as a lateral acceleration.
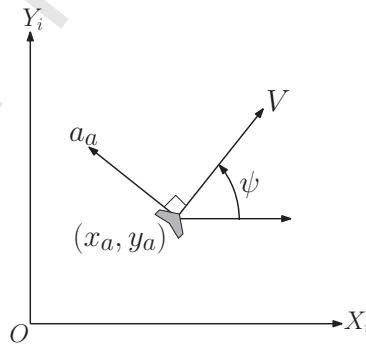

Figure 3: UAV motion in a fixed frame.

C. Pinhole Camera Model

Fig. 4 shows the standard pinhole camera model with the camera frame located at the pinhole of the camera. Axes, X_c and Y_c are defined along left and up, respectively. The
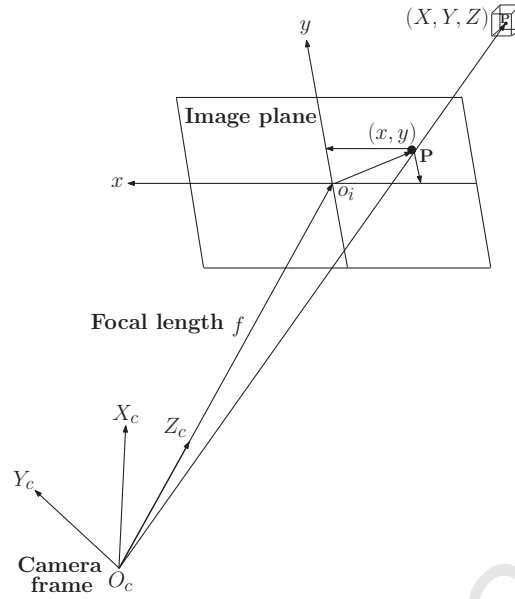
Figure 4: A pinhole camera model.

camera frame Z_c axis (also known as the optical axis) is perpendicular to the image plane. Note that, for a forward facing camera, Z_c coincides with the longitudinal axis of the UAV. Consider a point P in a 3D environment, the coordinates of which in the camera frame are $(X, Y, Z) \in \mathbb{R}^3$, projected in the image plane at the point $(x, y) \in \mathbb{R}^2$ given by

$$(x, y) = \left(\frac{fX}{Z}, \frac{fY}{Z} \right) \tag{4}$$

where, $f \in \mathbb{R}^+$ is the focal length of the camera.

III. Optical Flow

Optical flow is the apparent relative motion between a camera and the scene. Optical flow computation techniques can be broadly categorized into three types [25], namely: differential methods [26, 27], frequencey-based methods [28] and correlation-based methods [29]. Differential methods compute the spatio-temporal derivatives of image pixel brightness. Frequency-based methods are based on velocity-tuned filter, whereas correlation based methods compute velocity from local displacement of image features obtained from two consecutive frames. Although, correlation based methods are accurate, they suffer from periodic patterns. Due to robustness with respect to coarsely quantized images in space and time, the ability to handle additive noise and a lower computational demand differential methods provide a promising optical flow computation method [26]. One of the requirements of using a differential based is the differentiability of the image intensities. This work uses the differential method proposed by Horn and Schunck [26].

The optical flow method requires a sequence of gray level images to compute the optical flow vectors. Note that the images need to be filtered to increase the signal to noise ratio. In this work, a down sampling operation is used to filter the images.

A. Motion Framework

Consider the camera movement with respect to the 3D world with translational velocity (t_X, t_Y, t_Z) and angular velocity $(\omega_X, \omega_Y, \omega_Z)$.

Suppose a point moves by Δx and Δy in the x and y directions, respectively. The motion of the point in the image plane can be obtained from Eq. (4) as

$$\dot{x} = u = \frac{1}{Z}(-ft_X + xt_Z) - f\omega_Y + y\omega_Z + \frac{xy\omega_X}{f} - \frac{x^2\omega_Y}{f} \tag{5}$$

$$\dot{y} = v = \frac{1}{Z}(-ft_Y + yt_Z) - f\omega_X + x\omega_Z + \frac{xy\omega_Y}{f} - \frac{y^2\omega_X}{f} \tag{6}$$

where, Z is the depth of the point in $3D$ space relative to the camera; and u and v are the velocities of the point in the image plane located at (x, y) in the x and y directions, respectively.

B. Optical Flow Estimation

Horn-Schunck method [26] is used to compute the optical flow, where it is assumed that the brightness of the pixels in a frame does not vary with time. The method computes the motion between two image frames, captured at time instances t and $t + \Delta t$ at every pixel position where Δt is small. The method is based on gradients of image intensities of each pixel with respect to position and time.

A pixel at location (x, y, t) with intensity $I(x, y, t)$ moves by Δx, Δy and Δt between the two image frames. The following image constraint equation holds

$$I(x, y, t) = I(x + \Delta x, y + \Delta y, t + \Delta t) \tag{7}$$

Assuming that the movement of pixels from frame at t to frame at $t + \Delta t$ is small, the right side of Eq. (7) can be expanded using Taylor series expansion as

$$I(x, y, t) = I(x, y, t) + \frac{\partial I}{\partial x}\Delta x + \frac{\partial I}{\partial y}\Delta y + \frac{\partial I}{\partial t}\Delta t \tag{8}$$

which results in,

$$\frac{\partial I}{\partial x}u + \frac{\partial I}{\partial y}v + \frac{\partial I}{\partial t} = 0 \tag{9}$$

where, u and v represent the velocities in the x and y directions or optical flow of $I(x, y, t)$. Here, $\partial I/\partial x$, $\partial I/\partial y$ and $\partial I/\partial t$ are the partial derivatives of the image pixel located at

(x, y, t) in the x, y and t directions, and are denoted by I_x, I_y and I_t. From Eq. (9),

$$I_x u + I_y v = -I_t \tag{10}$$

which can be written as

$$\Delta I^T \cdot \vec{V} = -I_t \tag{11}$$

where, $\Delta I^T = [I_x, I_y]$ and $\vec{V} = [u, v]^T$. The quantities I_x, I_y, and I_t can be approximately computed as,

$$I_x \approx \frac{1}{4}(I_{i,j+1,k} - I_{i,j,k} + I_{i+1,j+1,k} - I_{i+1,j,k} + I_{i,j+1,k+1} - I_{i,j,k+1} + I_{i+1,j+1,k+1} - I_{i+1,j,k+1}) \tag{12}$$

$$I_y \approx \frac{1}{4}(I_{i+1,j,k} - I_{i,j,k} + I_{i+1,j+1,k} - I_{i,j+1,k} + I_{i+1,j,k+1} - I_{I,J,K+1} + I_{i+1,j+1,k+1} - I_{i,j+1,k+1}) \tag{13}$$

$$I_t \approx \frac{1}{4}(I_{i,j,k+1} - I_{i,j,k} + I_{i+1,j,k+1} - I_{i+1,j,k} + I_{i,j+1,k+1} - I_{i,j+1,k} + I_{i+1,j+1,k+1} - I_{i+1,j+1,k}) \tag{14}$$

where, $I_{i,j,k}$ is the gray level value of the pixel located at the ith row, j^{th} column, and k^{th} frame.

Eq. (11) has two unknowns and one equation and hence cannot be solved uniquely. This is known as the aperture problem [26]. In order to solve this problem, at least one more constraint equation is required. Horn and Schunck [26] assumed the optical flow field in each local region to be smooth. The measure of the deviation from smoothness in the optical flow is given by

$$J_s^2 = \left(\frac{\partial u}{\partial x}\right)^2 + \left(\frac{\partial u}{\partial y}\right)^2 + \left(\frac{\partial v}{\partial x}\right)^2 + \left(\frac{\partial v}{\partial y}\right)^2 \tag{15}$$

To compute the velocity vector the following cost function is minimized

$$J = \int \int (\alpha_w^2 J_s^2 + J_b^2) \, \mathrm{d}x \mathrm{d}y \tag{16}$$

where, α_w is a weighting factor and $J_b = I_t + I_x u + I_y v$. Suitable values of the optical flow velocities are obtained by minimization of the cost function. Using calculus of variations,

$$I_x^2 u + I_x I_y v = \alpha_w^2 \Delta^2 u - I_x I_t \tag{17}$$

$$I_x I_y u + I_y^2 v = \alpha_w^2 \Delta^2 v - I_y I_t \tag{18}$$

where, $\Delta^2 u = (\partial u/\partial x)^2 + (\partial u/\partial y)^2$ and $\Delta^2 v = (\partial v/\partial x)^2 + (\partial v/\partial y)^2$ are the Laplacians of the x and y components of the flow. Approximation of the Laplacians for u and v are given by the following equations:

$$\Delta^2 u \approx K(\overline{u}_{i,j,k} - u_{i,j,k}) \tag{19}$$

$$\Delta^2 v \approx K(\overline{v}_{i,j,k} - v_{i,j,k}) \tag{20}$$

where, $\overline{u}$ and $\overline{v}$ are the local averages of the velocities and are computed as follows:

$$\overline{u}_{i,j,k} = \frac{1}{6}(u_{i-1,j,k} + u_{i,j+1,k} + u_{i+1,j,k} + u_{i,j-1,k}) + \frac{1}{12}(u_{i-1,j-1,k} + u_{i-1,j+1,k} + u_{i+1,j+1,k} + u_{i+1,j-1,k}) \tag{21}$$

$$\overline{v}_{i,j,k} = \frac{1}{6}(v_{i-1,j,k} + v_{i,j+1,k} + v_{i+1,j,k} + v_{i,j-1,k}) + \frac{1}{12}(v_{i-1,j-1,k} + v_{i-1,j+1,k} + v_{i+1,j+1,k} + v_{i+1,j-1,k}) \tag{22}$$

After substituting the approximation of the Laplacians from the above equations in Eqs. (19) and (20), we get

$$(\alpha_w^2 + I_x^2 + I_y^2)(u - \overline{u}) = -I_x(I_x\overline{u} + I_y\overline{v} + I_t) \tag{23}$$

$$(\alpha_w^2 + I_x^2 + I_y^2)(v - \overline{v}) = -I_y(I_x\overline{u} + I_y\overline{v} + I_t) \tag{24}$$

Eqs. (23) and (24) can be solved iteratively for the velocity calculations as shown below,

$$u^{n+1} = \overline{u}^n - I_x \frac{I_x\overline{u}^n + I_y\overline{v}^n + I_t}{\alpha_w^2 + I_x^2 + I_y^2} \tag{25}$$

$$v^{n+1} = \overline{v}^n - I_y \frac{I_x\overline{u}^n + I_y\overline{v}^n + I_t}{\alpha_w^2 + I_x^2 + I_y^2} \tag{26}$$

where, (u^n, v^n) and (u^{n+1}, v^{n+1}) are the estimated velocities for the nth and $(n+1)^{th}$ frames, respectively. In the next subsection, Focus of Expansion point is calculated using the optical flow field.

C. Focus of Expansion

For a given translatory motion of the camera, the world seems to flow out from one point. This point is called the Focus of Expansion (FOE) in 3D world. The image is partitioned vertically into two sub-images from the FOE point. This point is computed from the optical flow field using a least square method [17][18]. The least square method is robust as it tries to find the best fit solution, which inherently discards the effect of optical flow vectors generated by noise. The FOE point can be detected by

$$(x_{foe}, y_{foe}) = (A^T A)^{-1} A^T b \tag{27}$$

where,

$$A_{p \times 2} = \begin{bmatrix} v_1 & -u_1 \\ \vdots & \vdots \\ v_i & -u_i \\ \vdots & \vdots \\ v_p & -u_p \end{bmatrix}, \qquad b_{p \times 1} = \begin{bmatrix} x_1 v_1 - y_1 u_1 \\ \vdots \\ x_i v_i - y_i u_i \\ \vdots \\ x_p v_p - y_p u_p \end{bmatrix} \tag{28}$$

where, p represents the total number of image pixels and i represents the ith pixel varies from 1 to p. The terms u and v are the optical flow velocities components in x and y directions, respectively.

Note that, FOE provides an accurate partition of the image even in the presence of side-slip. Canyon effect or urban structures can locally change the wind pattern which might result in non negligible side-slip. This motivates the use of FOE for image partition in the present work. However, FOE computations are based on optical flow and any errors therein can cause an erroneous partition of the image. It is assumed that the optical computation is reasonably accurate leading to a reliable FOE partition of the image. In the case of course optical flows or negligible side slip angles, center of the camera frame can be considered as an accurate and computationally feasible alternate partition logic for the image.

D. Optical Flow Computation

The following sequence of steps, based on the previous discussion, are carried out to compute the sum of the optical flow magnitudes for pixels on the left (OF^L) and right (OF^R) side sub-images to design the guidance strategy:

1. Sequence of color images captured by on-board camera are converted into gray level images.

2. The gray level images are down sampled to filter out the apparent noise from the images. The down sampling operation converts the high-resolution image to a lower resolution image and reduces the subsequent computation cost. There are various down-sampling approaches appearing in the literature. These include bilinear, bicubic, Lanczos, spline, and sinc-filter [19, 20]. The bilinear method presents a simple approach and requires a lower computation effort. Lanczos and spline methods improve the signal-to-noise ratio (SNR), however they are computationally expensive. Sinc-filters perform good in terms of SNR for smooth data. However, the method is prone to ripple artifacts in aliased images. On the other hand, bicubic method preserves the image sharpness with regional computations. Bicubic method is a preferable choice due to a good trade-off between image accuracy and processing time. In this work, bicubic approach is used to down-sample the images.

3. Optical flow velocities u and v are computed from Eqs. (25) and (26), respectively, which is further used to compute OF^L and OF^R as follows:

$$OF^L = \sum_{i=1}^{M} \sum_{j=1}^{y_{foe}} \sqrt{(u_{ij}^2 + v_{ij}^2)} \qquad (29)$$

$$OF^R = \sum_{i=1}^{M} \sum_{j=y_{foe}+1}^{N} \sqrt{(u_{ij}^2 + v_{ij}^2)} \qquad (30)$$

where, M and N denote the total number of rows and columns of an image, respectively. Here, y_{foe} represents the column value of the FOE point in the image.

IV. Optical Flow based Guidance

This section discusses the proposed inverse strategy and also presents the previously known balance strategy.

A. Inverse Strategy

The proposed strategy generates a guidance command using the inverse of the difference in optical flows as,

$$
\dot{\psi} = \begin{cases} \dfrac{\kappa_i}{(OF^R - OF^L)} & \text{if } \left|(OF^R - OF^L)\right| > C, \\[2ex] \dfrac{\kappa_i}{[\text{sign}(OF^R - OF^L)]C} & \text{if } \left|(OF^R - OF^L)\right| < C. \end{cases}
\tag{31}
$$

where, $C > 0$ is a constant term added to saturate the turn rate for very low optical flow differences, and $\kappa_i > 0$ is a proportionality constant. Here, $(OF^R - OF^L)$ is the difference in optical flows on the two sides of the UAV. For higher value of the right side optical flow, a positive value of guidance command turns the UAV to the left. Similarly, the UAV turns to the right for higher values of left side optical flow by generating a negative guidance command. Fig. 5 depicts the turning rates variation under the proposed law. It can
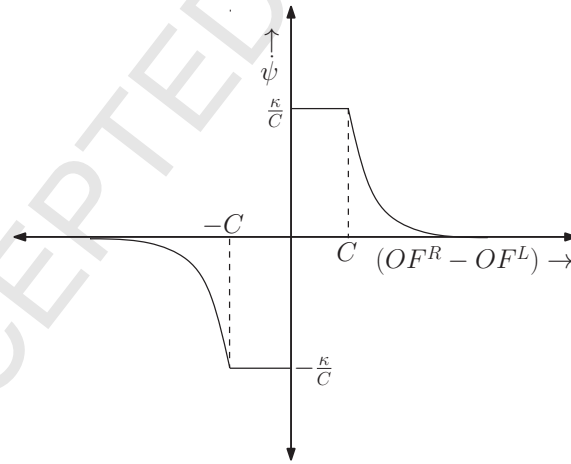

Figure 5: UAV turn rate command for proposed inverse strategy.

be seen that the strategy generates high turning rates for small optical flow differences. Since the UAV has limitation on its turn rate, $\dot{\psi}_{max}$ represents the maximum value of turn rate that the UAV can achieve. The constant C is selected such that the saturation value κ_i/C is equal to $\dot{\psi}_{max}$. For $(OF^R - OF^L) = 0$, the turn rate is equal to κ_i/C with the sign being the same as that of the previous optical flow difference.

B. Balance Strategy

Guidance command generated by balance strategy [3] is directly proportional to the optical flow difference between the two sides of the UAV,

$$\dot{\psi} = \kappa_b(OF^R - OF^L) \tag{32}$$

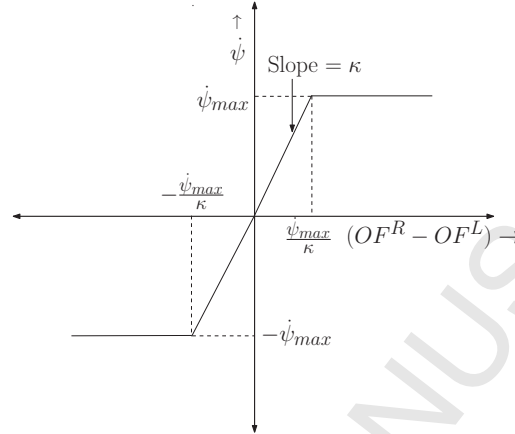where, $\kappa_b > 0$ is a proportionality constant. Fig. 6 plots turn rate against optical flow

Figure 6: UAV turn rate command for balance strategy.

difference for balance strategy. Here, $(\dot{\psi}_{max}/\kappa_b)$ denotes the value of optical flow difference for which the guidance command is equal to $\dot{\psi}_{max}$. The guidance command can be saturated to $\dot{\psi}_{max}$ for any $|OF^R - OF^L| \geq (\dot{\psi}_{max}/\kappa_b)$.

C. Comparison

To compare the two strategies, consider the scenarios shown in Fig. 7, FOV represents the camera field of view. In Fig. 7 (a), the UAV faces a side wall of the canyon, resulting in low optical flow difference, causing the inverse strategy to apply a high turn rate, preventing the UAV from crashing into the side wall. The balance strategy applies less turn rate, increasing the possibility of collision with the walls. In Fig. 7 (b), the UAV starts from Point **a**, where the FOV covers an approximately equal portion of the canyon, again resulting in low optical flow difference. As the UAV approaches point **b** (Fig. 7 (c)), FOV just clears the bend in the wall on the right side. At this point the optical flow from the left side of the FOV is higher than that from the right. At this point if the optical flow difference is insufficient, the UAV, using balanced strategy, will continue to move forward. When the UAV reaches Point **c** (Fig. 7 (d)), the optical flow difference will be even less than **b**, and the UAV will crash into the wall. In contrast, if the UAV uses the inverse strategy, at Point **b**, it will generate a high control force and turn the UAV into the right side corridor. Thus, the inverse strategy has an in-built robustness that eventually leads to successful collision avoidance. This behavior will be demonstrated

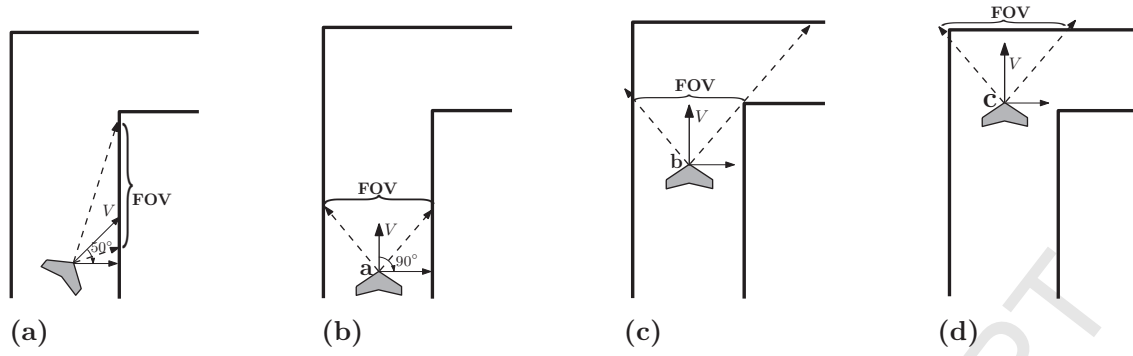**(a)**   **(b)**   **(c)**   **(d)**

Figure 7: UAV navigation through L shaped canyon for initial heading angle (a) to the right side (b) to the front, but UAV away from the bend (c) UAV close to the bend (d) UAV beyond the bend.

in the simulation and will be shown to be the core idea behind success of the inverse strategy over the balance strategy. However, this significant advantage often involves a jitter in the guidance command while having a low optical flow difference.

V.   Analysis of Optical Flow based Guidance Strategies

In this section, an analytic comparison of the inverse strategy and the balance strategy is carried out for a UAV directly approaching an obstacle. The analysis is performed for an infinite length wall followed by a finite sized obstacle.

A.   Infinite Length Wall

Consider a planar scenario, as shown in Fig. 8, where a UAV, flying with an initial angle ψ, faces an infinite length wall. The fixed frame x axis (X_i) is chosen along the normal going into the wall and Y_i completes the right handed system. To avoid a collision with the wall, the UAV must attain a heading

$$|\psi| \geq \frac{\pi}{2} \quad \text{for an} \quad X_{rel} > 0 \tag{33}$$

where, $X_{(rel)}$ is the separation between the camera (or UAV) and the obstacle along X_i. The point T on the obstacle is projected on the center of the image. In order to calculate OF^R and OF^L the image is partitioned vertically from the center. The camera horizontal field-of-view is denoted by α. The optical flow velocities in the x and y directions are calculated using (5) and (6), with

$$t_X = \dot{y}_a = V \sin \psi \tag{34}$$
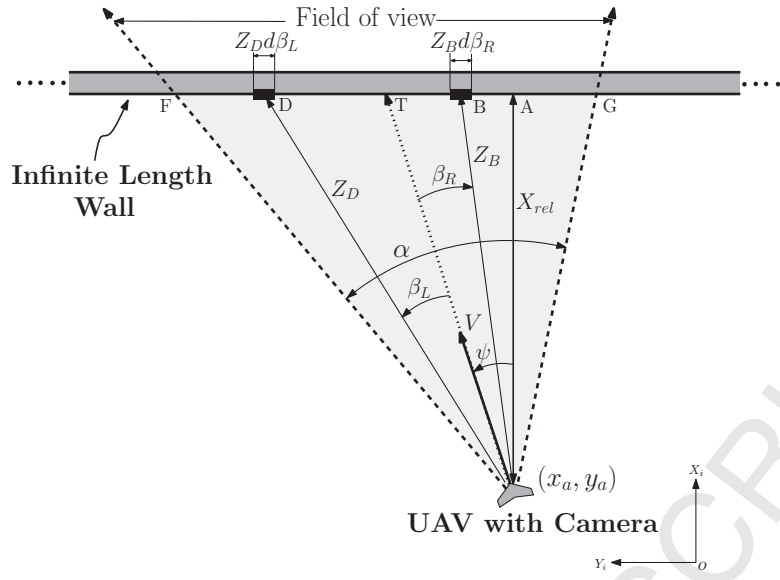
$$t_Z = \dot{x}_a = V \cos \psi \tag{35}$$

Figure 8: A UAV facing an infinite length wall.

$$\omega_Y = \dot{\psi} = \frac{a_a}{V} \tag{36}$$

$$t_Y = \omega_X = \omega_Z = 0. \tag{37}$$

to obtain

$$u = \frac{V}{Z}(-f \sin \psi + x \cos \psi) - \frac{f a_a}{V} - \frac{x^2 a_a}{f V} \tag{38}$$

$$v = \frac{V y \cos \psi}{Z} + \frac{x y a_a}{f V} \tag{39}$$

Fig. 8 shows that the right and left side sub-images project the obstacle from the points G to T and T to F, respectively. Assume a point D is located at an angle β_L on the left side sub-image. The magnitude of the optical flow for point D can be written as

$$OF_D = \sqrt{u^2 + v^2} \tag{40}$$

For the planar engagement, horizontal field-of-view is considered with $y = 0$, which further simplifies Eq. (40) as

$$OF_D = u \tag{41}$$

Substituting u from Eq. (38) in Eq. (41), with $x = f \tan \beta_L$, leads to

$$OF_D = \frac{fV}{Z_D}(-\sin \psi + \tan \beta_L \cos \psi) - \frac{f a_a}{V} - \frac{f(\tan \beta_L)^2 a_a}{V} \tag{42}$$

where, Z_D is the depth of the point D from the UAV given by

$$Z_D = \frac{X_{rel}}{\cos(\beta_L + \psi)} \tag{43}$$

and

$$X_{rel} = X_{(rel)_0} - \int V \cos\psi \, dt \tag{44}$$

Here, $X_{(rel)_0}$ is the initial separation between the camera (or UAV) and the obstacle. Substituting Z_D from Eq. (43) in Eq. (42), yields

$$OF_D = \frac{Vf\cos(\beta_L + \psi)}{X_{rel}}(-\sin\psi + \tan\beta_L \cos\psi) - \frac{fa_a}{V} - \frac{f(\tan\beta_L)^2 a_a}{V} \tag{45}$$

To calculate the optical flow for all the points projected on the left side sub-image, the optical flow governed by Eq. (45) is integrated with respect to β_L over the limits 0 to $\alpha/2$ as

$$OF^L = \int_0^{\alpha/2} (OF_D) \, d\beta_L \tag{46}$$

Using (45) in (46),

$$OF^L = \int_0^{\alpha/2} \left(\frac{Vf\cos(\beta_L + \psi)}{X_{rel}}(-\sin\psi + \tan\beta_L \cos\psi) - \frac{fa_a}{V} - \frac{f(\tan\beta_L)^2 a_a}{V} \right) d\beta_L \tag{47}$$

which, on further simplification, yields

$$OF^L = \frac{Vf}{X_{rel}}\left(1 - \cos\frac{\alpha}{2} - \sin\psi\cos\psi \ln\left|\sec\frac{\alpha}{2} + \tan\frac{\alpha}{2}\right|\right) - \frac{a_a f}{V}\tan\frac{\alpha}{2} \tag{48}$$

Similarly, OF^R for the right sub-image can be computed as

$$OF^R = \int_0^{\alpha/2} (OF_B) \, d\beta_R \tag{49}$$

where, OF_B represents the optical flow magnitude of the point B at an angle β_R on the right side sub-image. By using $x = -f\tan\beta_R$, OF_B can be expressed as

$$OF_B = \frac{fV}{Z_B}(-\sin\psi - \tan\beta_R \cos\psi) - \frac{fa_a}{V} - \frac{f(\tan\beta_R)^2 a_a}{V} \tag{50}$$

From Fig. 8,

$$Z_B = \frac{X_{rel}}{\cos(\psi - \beta_R)} \tag{51}$$

Using (50) in (51),

$$OF_B = \frac{Vf\cos(\beta_R - \psi)}{X_{rel}}(-\sin\psi - \tan\beta_R\cos\psi) - \frac{fa_a}{V} - \frac{f(\tan\beta_R)^2 a_a}{V} \qquad (52)$$

Substitution of OF_B from (52) in (49), leads to

$$OF^R = \frac{Vf}{X_{rel}}\left(\cos\frac{\alpha}{2} - 1 - \sin\psi\cos\psi\ln\left|\sec\frac{\alpha}{2} + \tan\frac{\alpha}{2}\right|\right) - \frac{a_a f}{V}\tan\frac{\alpha}{2} \qquad (53)$$

The difference of the right and left side optical flow can be computed as

$$OF^R - OF^L = \frac{2Vf\left(\cos\dfrac{\alpha}{2} - 1\right)}{X_{rel}} \qquad (54)$$

1. Inverse Strategy

Substituting the optical flow difference from Eq. (54) in Eq. (31) for $(OF^R - OF^L) > C$, the turn rate command for the inverse strategy can be obtained as,

$$\dot{\psi} = \frac{\kappa_i X_{rel}}{2Vf\left(\cos\dfrac{\alpha}{2} - 1\right)} \qquad (55)$$

Variation in X_{rel} is governed by

$$\dot{X}_{rel} = -V\cos\psi \qquad (56)$$

Note that, the variation of ψ with respect to X_{rel} governs the obstacle avoidance behavior. The relation can be obtained by solving, in closed-form, the system governed by (55) and (56) as

$$\frac{\dot{X}_{rel}}{\dot{\psi}} = -\frac{2V^2 f\left(\cos\dfrac{\alpha}{2} - 1\right)\cos\psi}{\kappa_i X_{rel}} \qquad (57)$$

$$\Rightarrow \int (X_{rel})\,\mathrm{d}X_{rel} = -\frac{2V^2 f\left(\cos\dfrac{\alpha}{2} - 1\right)}{\kappa_i}\int \cos\psi\,\mathrm{d}\psi \qquad (58)$$

resulting in

$$\frac{X_{rel}^2}{2} = -\frac{2V^2 f\sin\psi\left(\cos\dfrac{\alpha}{2} - 1\right)}{\kappa_i} + C_I \qquad (59)$$

where, C_I is the integration constant given as

$$C_I = \frac{X_{(rel)_0}^2}{2} + \frac{2V^2 f\sin\psi_0\left(\cos\dfrac{\alpha}{2} - 1\right)}{\kappa_i}. \qquad (60)$$

where, ψ_0 represents the UAV initial heading angle.

2. Balance Strategy

Analytic relation between the X_{rel} and ψ using balance strategy can be obtained by substituting the optical flow difference from Eq. (54) in Eq. (32) as

$$\dot{\psi} = \frac{2Vf\kappa_b \left(\cos\dfrac{\alpha}{2} - 1 \right)}{X_{rel}} \tag{61}$$

Using (56) and (61),

$$\int \frac{dX_{rel}}{X_{rel}} = -\frac{1}{2f\kappa_b \left(\cos\dfrac{\alpha}{2} - 1 \right)} \int \cos\psi \, d\psi$$

$$\Rightarrow \ln|X_{rel}| = -\frac{\sin\psi}{2f\kappa_b \left(\cos\dfrac{\alpha}{2} - 1 \right)} + C_B \tag{62}$$

Here, C_B is the integration constant given by

$$C_B = \ln\left|X_{(rel)_0}\right| + \frac{\sin\psi_0}{2f\kappa_b \left(\cos\dfrac{\alpha}{2} - 1 \right)} \tag{63}$$

Eqs. (59) and (62) show the closed-form relation between ψ and X_{rel} using the inverse and balance strategies, respectively.

B. Finite Length Wall

Consider a scenario, where the UAV faces a finite length wall as shown in Fig. 9. Here, ψ_d represents the desired heading to avoid the wall. The avoidance can be guaranteed by achieving

$$|\psi| > |\psi_d| \quad \text{for an} \quad X_{rel} > 0 \tag{64}$$

Unlike the infinite wall case, the camera image plane may not be fully covered by the wall. Hence, to compute OF_L, Eq. (47) is integrated with respect to β_L over the limits 0 to δ_L. The limit δ_L is based on the obstacle position in the left half sub-image, given as

$$\delta_L = \begin{cases} \dfrac{\alpha}{2} & \text{if } \delta \geq \dfrac{\alpha}{2}, \\[2mm] \delta & \text{if } 0 < \delta < \dfrac{\alpha}{2}, \\[2mm] 0 & \text{if } \delta \leq 0. \end{cases} \tag{65}$$
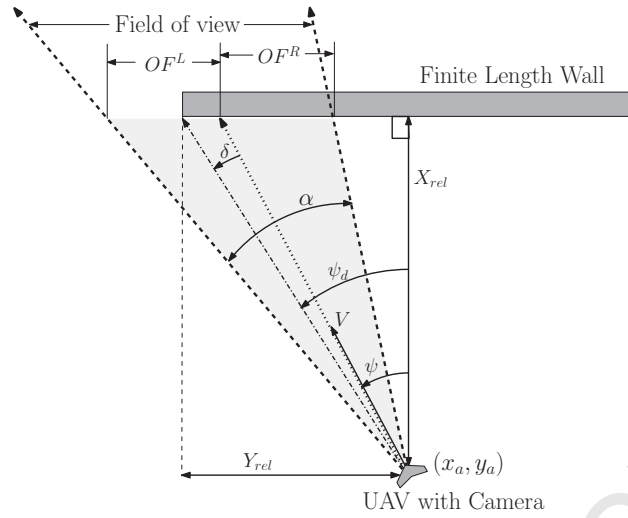
where,

$$\delta = \psi_d - \psi, \tag{66}$$

Figure 9: A UAV facing a finite length wall.

$$\psi_d = \tan^{-1}\left(X_{rel}/Y_{rel}\right) \tag{67}$$

and

$$Y_{rel} = Y_{(rel)_0} - \int V \sin\psi \, dt \tag{68}$$

here, $Y_{(rel)_0}$ is the initial separation between the camera (or UAV) and the obstacle edge along Y_i. Using the new limit in (47), results in

$$OF^L = \frac{Vf}{X_{rel}}(1 - \cos\delta_L - \sin\psi\cos\psi\ln|\sec\delta_L + \tan\delta_L|) - \frac{a_a f}{V}\tan\delta_L \tag{69}$$

Similarly, OF^R can be computed using (49) by taking the integral of β_R over the limits 0 to δ_R,

$$OF^R = \frac{Vf}{X_{rel}}(\cos\delta_R - 1 - \sin\psi\cos\psi\ln|\sec\delta_R + \tan\delta_R|) - \frac{a_a f}{V}\tan\delta_R \tag{70}$$

where,

$$\delta_R = \begin{cases} \dfrac{\alpha}{2} & \text{if } \delta > 0, \\[2mm] \left(\dfrac{\alpha}{2} + \delta\right) & \text{if } -\dfrac{\alpha}{2} < \delta \le 0, \\[2mm] 0 & \text{if } -\dfrac{\alpha}{2} \ge \delta. \end{cases} \tag{71}$$

The difference of the right and left side sub-images optical flows is

$$\begin{aligned} OF^R - OF^L = {} & \frac{Vf}{X_{rel}}\left(\cos\delta_R + \cos\delta_L - 2 - \sin\psi\cos\psi\ln\left|\frac{\sec\delta_R + \tan\delta_R}{\sec\delta_L + \tan\delta_L}\right|\right) \\ & -\frac{a_a f}{V}(\tan\delta_R - \tan\delta_L) \end{aligned} \tag{72}$$

1. Inverse Strategy

To compute the expression for turn rate when $(OF^R - OF^L) > C$, the optical flow difference from Eq. (72) is substituted in Eq. (31) to obtain

$$\dot{\psi} = \frac{\kappa_i}{\dfrac{Vf}{X_{rel}}\left(\cos\delta_R + \cos\delta_L - 2 - \sin\psi\cos\psi\ln\left|\dfrac{\sec\delta_R + \tan\delta_R}{\sec\delta_L + \tan\delta_L}\right|\right) - \dfrac{a_a f}{V}(\tan\delta_R - \tan\delta_L)} \tag{73}$$

The remaining state equations are given as

$$\dot{X}_{rel} = -V\cos\psi \tag{74}$$

$$\dot{Y}_{rel} = -V\sin\psi \tag{75}$$

Unlike (55)-(56), Eqs. (73)-(75), cannot be solved analytically. The solution can be obtained by numerical integration.

2. Balance Strategy

Here, $\dot{\psi}$ can be computed by substituting the optical flow difference from Eq. (72) in Eq. (32) as

$$\dot{\psi} = \kappa_b\left(\frac{Vf}{X_{rel}}\left(\cos\delta_R + \cos\delta_L - 2 - \sin\psi\cos\psi\ln\left|\frac{\sec\delta_R + \tan\delta_R}{\sec\delta_L + \tan\delta_L}\right|\right)\right.$$
$$\left. - \frac{a_a f}{V}(\tan\delta_R - \tan\delta_L)\right) \tag{76}$$

Eq. (76) is a coupled nonlinear differential equation and cannot be separated. The system governed by (74)-(76) need to solved numerically, like the infinite wall case.

C. Comparisons

Consider a UAV flying from an initial position $(2, 0.5)$ m with an initial heading angle $\psi_0 = 2°$. The UAV flies with a constant speed of 1 m/s with maximum turn rate of $\dot{\psi}_{max} = 0.5$ rad/s. The initial separation between the UAV and the wall is $X_{(rel)_0} = 2$ m, and the initial lateral separation between the UAV and the obstacle edge is $Y_{(rel)_0} = 0.5$ m. Fig. 10 (a) shows the UAV trajectories for an infinite wall case. Resultant trajectory represented by the solid line, generated using (59), (74) and (75), shows that the inverse strategy steers the UAV away from the wall. On the other hand, the trajectory (represented by doted line) generated using (62), (74) and (75), for the balance strategy, shows that the UAV collides with the wall. This is due to the low turn maneuver applied by the balance strategy. The corresponding heading variation is shown in Fig. 10 (b). Inverse strategy attains the desired heading given by (33), whereas the balance strategy fails to achieve. A similar result is obtained using (73)-(76) for a finite wall case as shown in
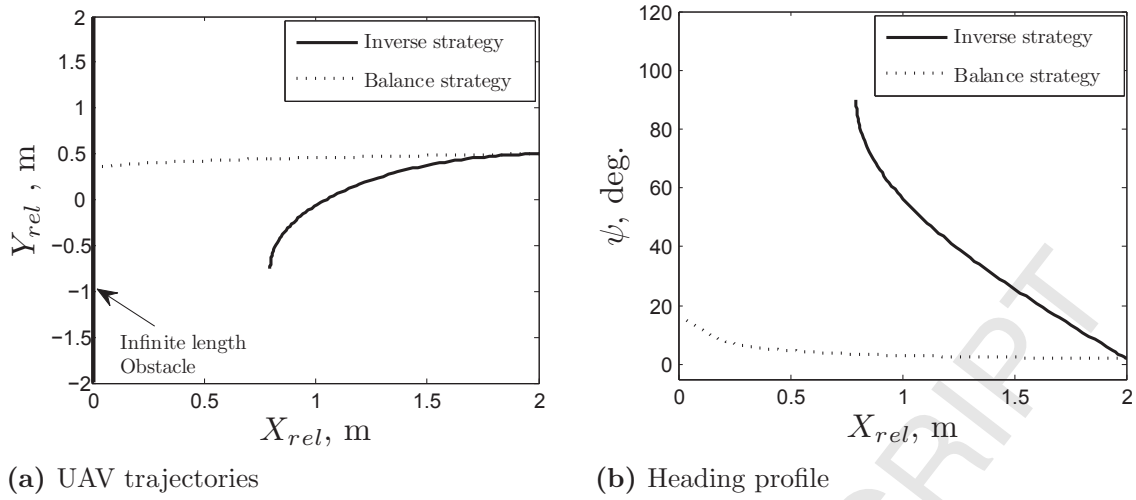
18 of 31

(a) UAV trajectories

(b) Heading profile

Figure 10: Results for infinite length wall.

Fig. 11 (a). The corresponding heading variation is shown in Fig. 11 (b). As illustrated in

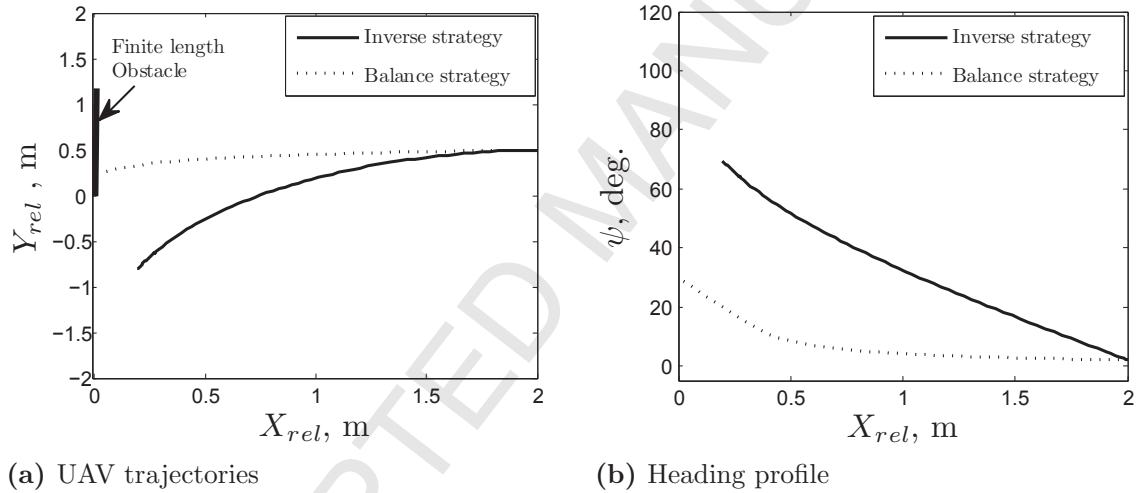**(a)** UAV trajectories

(b) Heading profile

Figure 11: Results for finite length wall.

Fig. 11 (a), the UAV is able to avoid the finite wall using the inverse strategy by achieving the heading governed by (64). In contrast, the balance strategy fails to satisfy the condition given in (64). Analytical results highlight the superiority of inverse strategy in safely avoiding directly facing obstacles.

VI. Simulation Results

Simulation studies are carried out in a virtual 3D environment created using virtual reality modelling languages (VRML) in MATLAB. For simulations, point mass and 6 DoF UAV models are used, where the UAV is equipped with a forward facing pinhole camera with $80° \times 80°$ field of view. After down sampling, the resolution of the image is

150×150 pixels, (256 gray level). The point mass model of the UAV flies with a constant speed of 1 m/s with a camera capturing 10 frames per seconds and and a maximum turn rate $\dot{\psi}_{max} = 0.25$ rad/s. A real texture image, as shown in Fig. 12 (a), is used to construct obstacles. Note that optical flow computation accuracies depend on the obstacle surface texture. Accuracy of optical flows reduces for poor textured surfaces such as solid-coloured surfaces or fine-grained patterns. For accurate optical flow values, the obstacle should have significantly textured surfaces [30, 31]. In this work, we assume that the urban environments are sufficiently rich in texture. Simulation studies are carried out for straight, L and T shape canyons and their combinations. Noise due to camera measurement is additive gaussian noise with zero mean and a variance ranging typically from 0.01 to 0.05 [32, 33]. To check the robustness of the proposed strategy with respect to camera measurement error, the images are corrupted by additive gaussian noise with zero mean and 0.03 variance.

(a) A real texture image

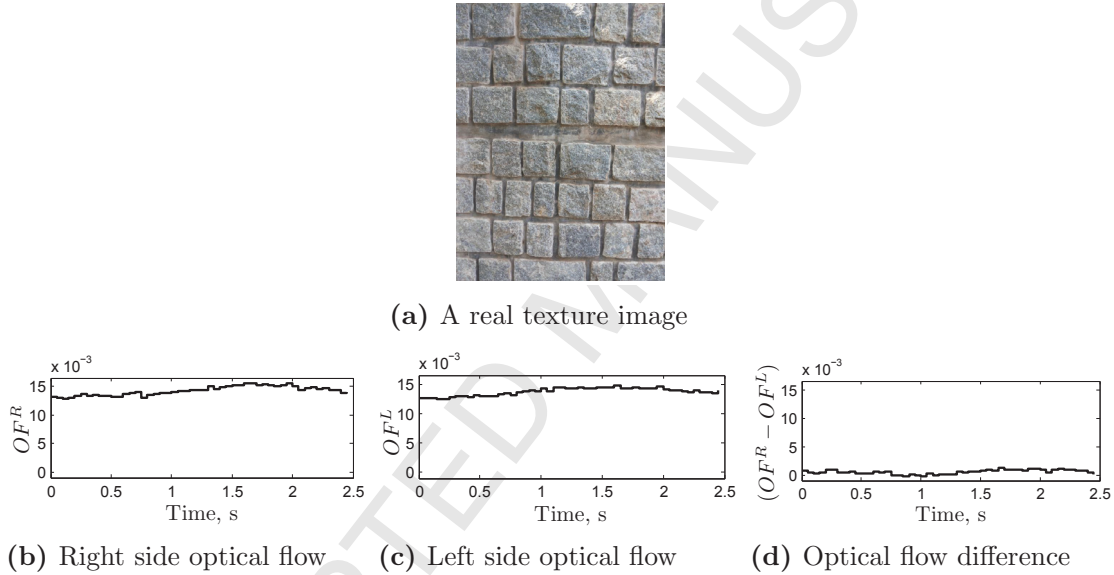(b) Right side optical flow   (c) Left side optical flow   (d) Optical flow difference

Figure 12: A real texture image and corresponding optical flow profiles.

Note that the $(OF^R - OF^L) = 0$ when the optical flow on both sides of the UAV are equal. However, in practical scenarios, this does not happen due to noise and asymmetry in texture. To show the asymmetry in optical flow on both sides of the texture image used in this work, consider a scenario in which UAV faces the center of the wall constructed using the image shown in Fig. 12 (a), and flies towards the wall without using any guidance. Figs. 12 (b) and (c) show the right and left side optical flows, respectively. Their difference is shown in Fig. 12 (d). Note that the jittering in optical flow is due to noise, whereas the difference in optical flow is due to asymmetry in the image texture.

Simulation studies for Case 1 to 5 are carried out using the point mass model of the UAV, whereas in Case 6 a high fidelity 6DoF UAV model is considered.

Case 1: Single Obstacle

Fig. 13 (a) shows the scenario, where the obstacle dimensions are 1 m × 1 m. The UAV faces the obstacle from an initial position $(0, 0.5)$ m and heading angle, $\psi_0 = 2°$. Resultant trajectories of the UAV using the inverse and the balance strategies are shown in Fig. 13 (b). Results show that the UAV navigates safely using the inverse strategy,
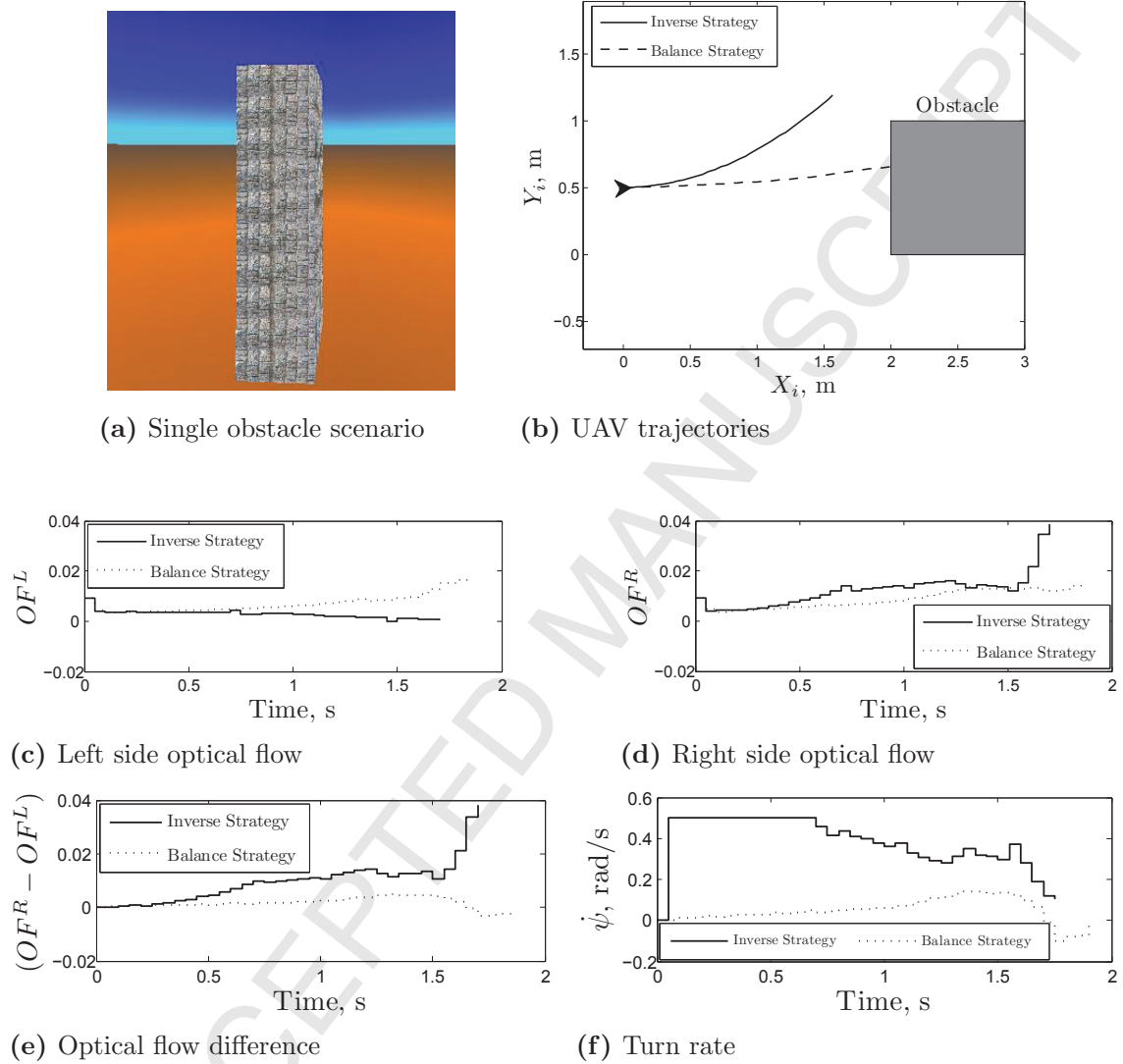

(a) Single obstacle scenario

(b) UAV trajectories

(c) Left side optical flow

(d) Right side optical flow

(e) Optical flow difference

(f) Turn rate

Figure 13: Results for Case 1 ($\psi_0 = 2°$).

whereas the balance strategy fails to avoid the obstacle. Figs. 13 (c) and (d) show the left and right side optical flows, respectively. Their differences and corresponding guidance commands are shown in Figs. 13 (e) and (f), respectively. Note that the inverse strategy initially generates a high turn rate. This is due to less difference in optical flow, resulting in a safe navigation of the UAV. On the other hand, the balance strategy generates low turn rate and fails to navigate the UAV safely.

Case 2: Straight Canyon

Fig. 14 shows a straight canyon with two 24 m long parallel walls separated by 6 m. The
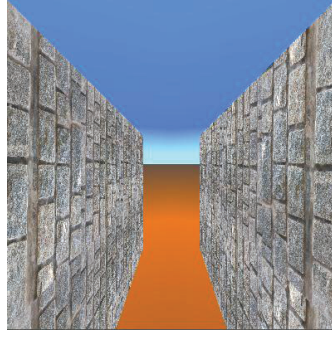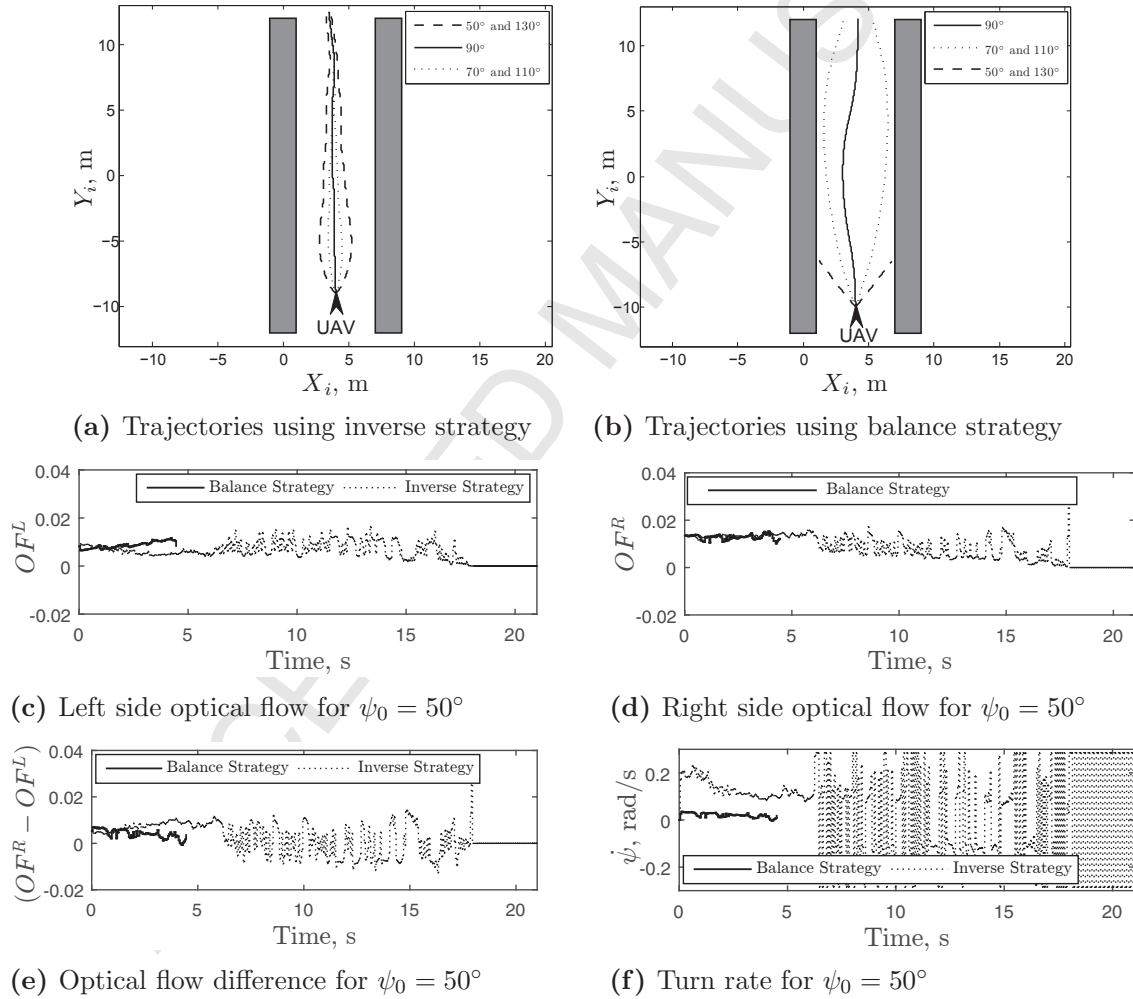

Figure 14: Straight canyon scenario created in VRML.

(a) Trajectories using inverse strategy

(b) Trajectories using balance strategy

(c) Left side optical flow for $\psi_0 = 50°$

(d) Right side optical flow for $\psi_0 = 50°$

(e) Optical flow difference for $\psi_0 = 50°$

(f) Turn rate for $\psi_0 = 50°$

Figure 15: Results for Case 2.

UAV starts from $(3, -11, 3)$ m. UAV trajectories for the initial heading angle $\psi_0 = 50°$ are shown by dashed lines in Figs. 15 (a) and (b), respectively. Result shows that the

UAV navigates safely using the inverse strategy. In contrast, the balance strategy fails to generate enough turn rate. Figs. 15 (c) and (d) show the left and right side optical flows, respectively. Their differences and corresponding guidance command are shown in Figs. 15 (e) and (f), respectively.

For further comparison between both the strategies, the UAV is set to different initial heading angles between 0° to 180°. It is found that the inverse strategy navigates the UAV safely for the range of initial heading angles of 45.3° to 135.4°, whereas the balance strategy achieves safe navigation of the UAV only for initial heading angles from 68.8° to 111.6°. The slight asymmetry in the safe heading angles on both sides of the center line is due to the non-homogeneity in the image texture of the two walls used in VRML. For an
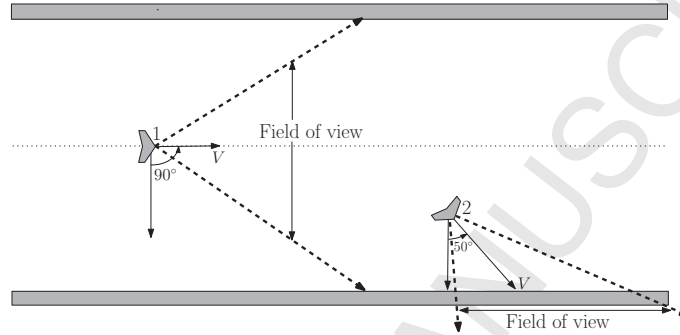

Figure 16: UAV heading scenarios moving through a canyon.

insight into the comparative behavior, consider the scenario, as shown in Fig. 16, where the UAV is located at two different positions along the canyon. Although the difference in optical flows is less for both the positions, the UAV at Position 2 requires a high turn maneuver to avoid a collision. The balance strategy fails to differentiate between the two situations and generates a low turn rate command. This leads to a collision with the wall as shown in Fig. 15 (b) for the headings 50° and 130°. In comparison, the inverse strategy avoids the wall by applying a high turn maneuver.

Case 3: L Shape Canyon

The top view of the L shape canyon is shown in Fig. 17. Consider the scenario, where the UAV flies from $(3.5, -7, 3)$ m at an initial heading of $\psi_0 = 110°$. Figs. 18 (a) and (b) show the UAV navigation trajectories using the inverse and balance strategies (as represented by solid line), respectively. Figs. 18 (e) and (f) show the optical flow difference and the corresponding guidance command, respectively. Note that the UAV initially faces the left side wall of the canyon, which results in a small negative optical flow difference. Due to the small difference, the inverse strategy generates a high turn rate during $t = 0$ s to $t_1 = 0.75$ s, as shown in Fig. 18 (f). This turns the UAV to face along the center of the canyon. As time progresses from $t_1 = 0.75$ s to $t_2 = 7.6$ s, the turn rate switches with the respective switching in the optical flow difference. Finally, between $t_2 = 7.6$ s to $t_3 = 9.8$
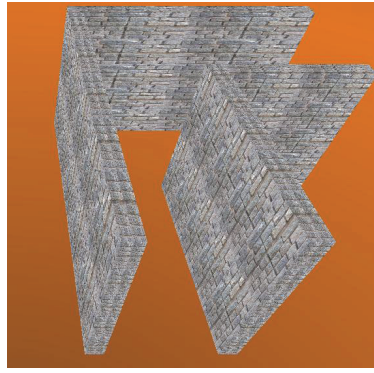
Figure 17: L-shape canyon scenario created in VRML.

(a) Trajectories using inverse strategy

(b) Trajectories using balance strategy

(c) Left side optical flow for $\psi_0 = 110°$

(d) Right side optical flow for $\psi_0 = 110°$

(e) Optical flow difference for $\psi_0 = 110°$

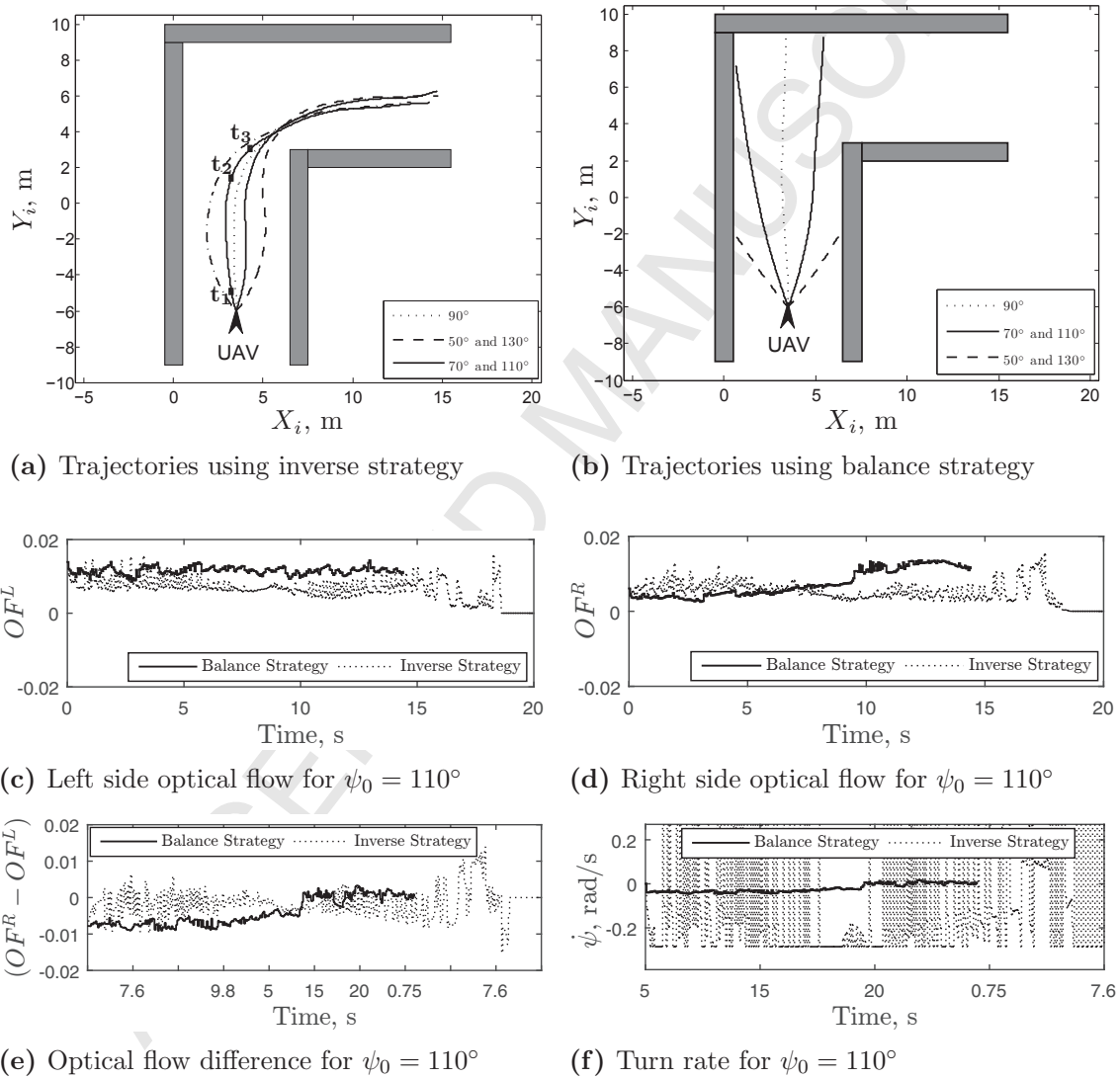

(f) Turn rate for $\psi_0 = 110°$

Figure 18: Results for Case 3.

s, the UAV turns right by applying a high turn rate. In contrast, the balance strategy generates lower turn rate, which results in collision. Using the inverse strategy, the UAV

navigates safely for all initial heading angles from 47° to 150°. Note that in Fig. 18 (b), some trajectories in balance strategy fail as they collide with the side wall and the others due to collision with the front wall.

Effect of roll angle

Simulation in Cases 1-3 assume a constant speed point mass model for the UAV moving in a plane. For following the desired turn rate command the UAV requires a bank angle. With bank angle, the partitioning of the image no longer vertical unless the camera is mounted on gimbals. Additional simulations are carried out for studying the effect of roll angle on the performance of the proposed method. Consider the same L shaped canyon as in Case 3. The UAV has an initial heading angle of ($\psi_0 = 100°$). The bank angle ϕ can be related to turn rate for a level flight as

$$\phi = \tan^{-1}\left(\frac{\dot{\psi}v}{g}\right) \tag{77}$$

Using Eq. (77), the maximum bank angle for the considered maximum turn rate of 0.25 rad/s can be obtained to be 0.0255 radians (1.461 degrees). Trajectories are plotted
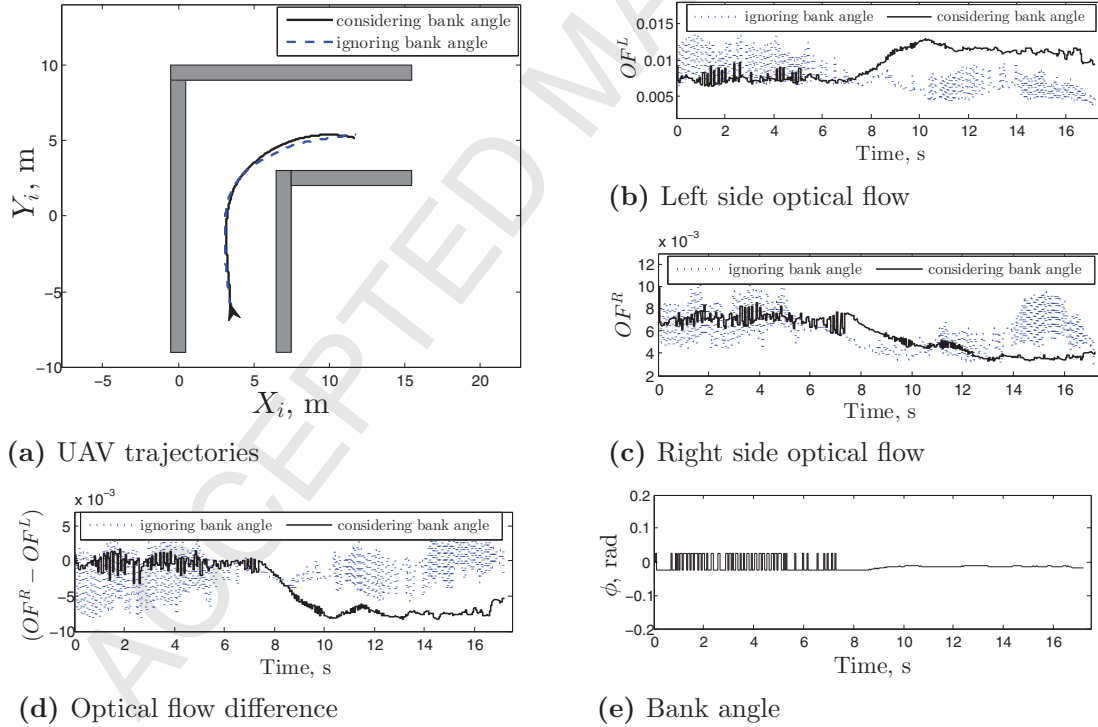

(a) UAV trajectories

(b) Left side optical flow

(c) Right side optical flow

(d) Optical flow difference

(e) Bank angle

Figure 19: Effect of roll angle ($\psi_0 = 100°$).

in Fig. 19 (a). The corresponding optical flows and their differences are plotted in Figs. 19 (b) - (d) and Fig. 19 (e) plots the UAV bank angle. Results present a close match with those obtained ignoring a bank-to-turn requirement. However, very high values of

bank angle can lead to an erroneous vertical partition of the image and deterioration of the performance.

Case 4: T Shape Canyon

Fig. 20 shows a T-shaped canyon. The UAV starts from $(0, -6, 3)$ m. Consider the UAV passing through the canyon for the initial heading, $\psi_0 = 90°$. Resultant trajectories using
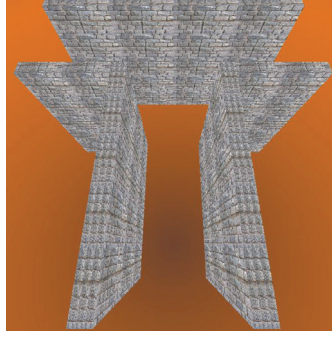

Figure 20: T-shape canyon scenario created in VRML.

inverse and balance strategies are shown by the solid line in Figs. 21 (a) and (b), respectively. The optical flow difference and corresponding turn rates are shown in Figs. 21 (c) and (d), respectively. Note that the inverse strategy applies a high turn rate between

(a) Trajectories using inverse strategy

(b) Trajectories using balance strategy
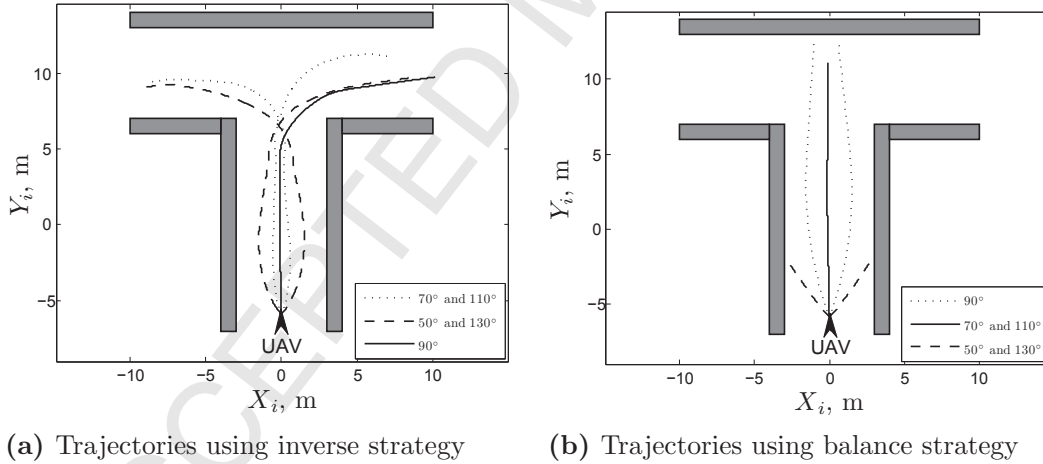
$t_2 = 10$ s to $t_3 = 16$. Using inverse strategy, the UAV has a safe navigation for initial heading angles from $27.8°$ to $151.5°$, whereas the balance strategy fails for all the initial heading angles.

Case 5: Combination of L and T Shaped Canyons

Fig. 22 (a) shows a top view of a scenario which is a combination of T and L shape canyons. Fig. 22 (b) shows the UAV trajectory for 25 different headings chosen randomly from the range $30°$ to $150°$. Results show that the inverse strategy based guidance
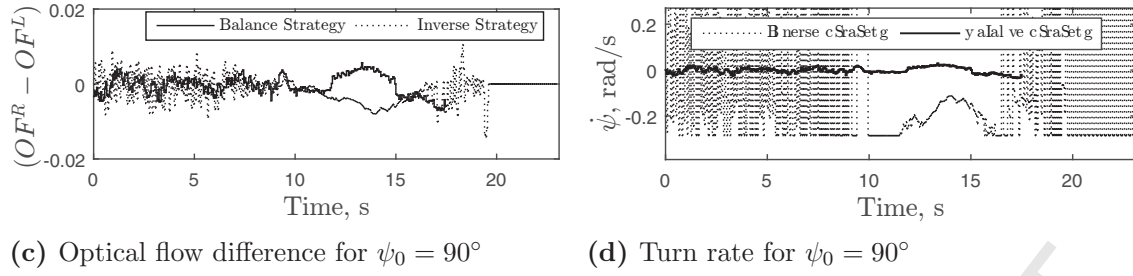
(c) Optical flow difference for $\psi_0 = 90°$

(d) Turn rate for $\psi_0 = 90°$

Figure 21: Results for Case 4.

(a) Trajectories using inverse strategy

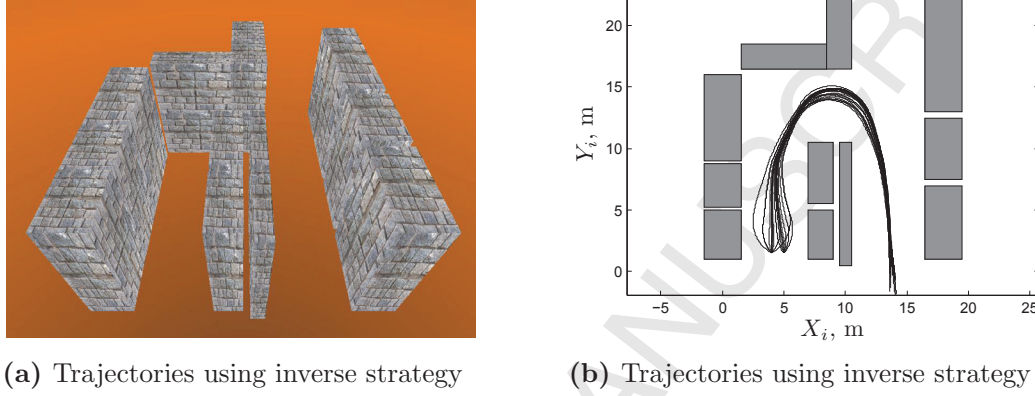**(b)** Trajectories using inverse strategy

Figure 22: Results for Case 5.

navigates the UAV successfully through complex and realistic scenarios. In contrast, the balance strategy fails for all the initial conditions, and the trajectories are not included here.

Case 6: L Shape Canyon with 6 DoF UAV Model

An L shape canyon, as shown in Fig. 23 (a), is considered to validate the proposed strategy using a high fidelity six degree-of-freedom UAV model. The dynamics is modelled by the six degree-of-freedom flight equations for Zagi MAV [34]. The UAV speed is held constant at $V = 10.5$ m/s by the velocity hold controller. The minimum turn radius of the UAV is 75 m. The camera captures images at 100 Hz. Consider that the UAV flies through the canyon from $(40, -90, 49)$ m with an initial heading $\psi_0 = 130°$ and 5° pitch angle as shown in Fig. 23 (a). UAV trajectories show that the UAV successfully navigates through the canyon using the inverse strategy, whereas balance strategy fails to avoid the front wall. Figs. 23 (b) and (c) show the left and right sides optical flow using the inverse strategy, respectively. The optical flow difference is shown in Fig. 23 (d). The corresponding turn rate commands are shown in Fig. 23 (e). Note that initially the UAV avoids the left side wall of the canyon. As time progresses, the UAV approaches the front wall and applies a negative high turn rate, avoiding the front wall. Fig. 24 shows the UAV states and the

(a) UAV trajectories

(b) Left side optical flow

(c) Right side optical flow

(d) Optical flow difference

(e) Turn rate
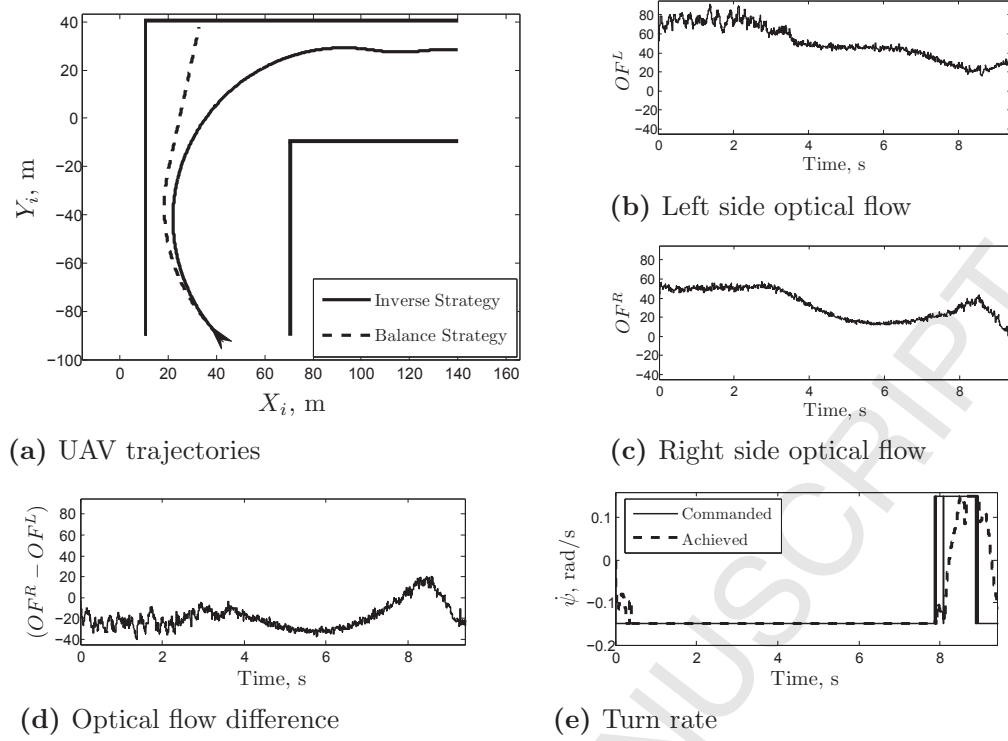
Figure 23: Results for Case 6 using inverse strategy ($\psi_0 = 130°$).

(a) Heading profile

(b) Velocity profile

(c) Altitude profile

(d) Throttle input

(e) Aileron input

(f) Elevator input

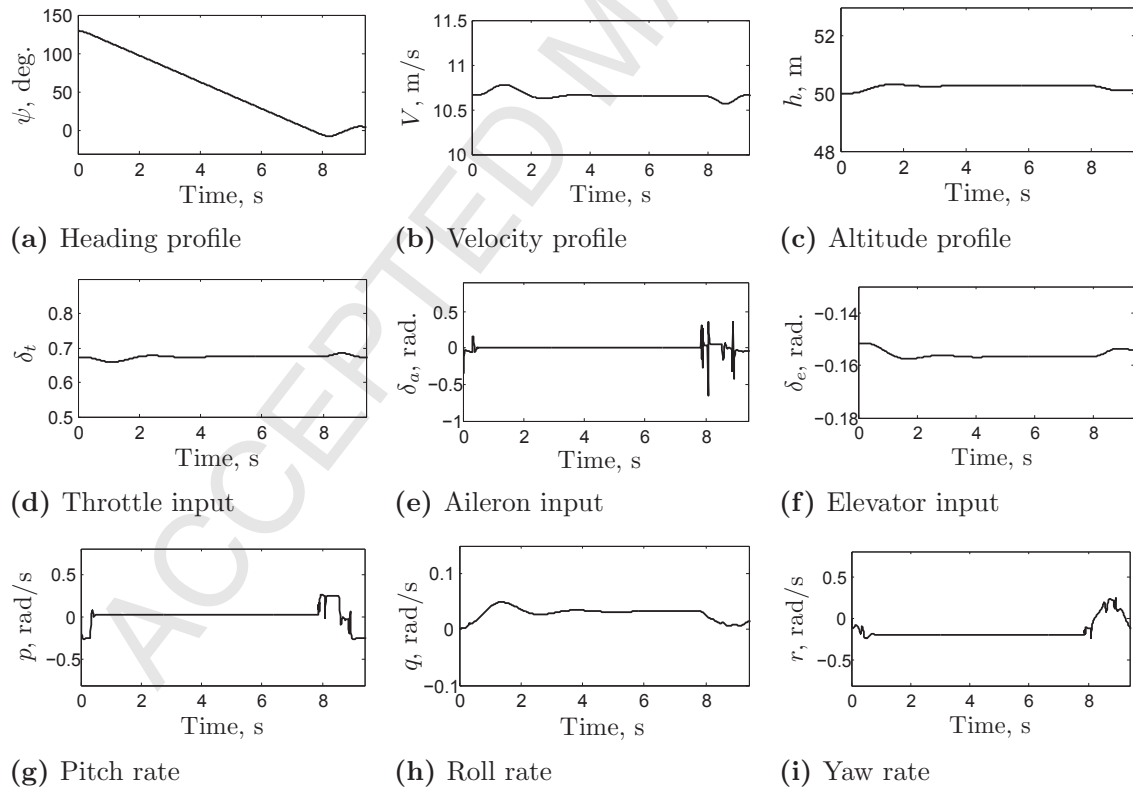(g) Pitch rate

(h) Roll rate

(i) Yaw rate

Figure 24: Vehicle states and control histories for Case 6.

control histories using the inverse strategy. Fig. 24 (a) shows the heading angle profile. Figs. 24 (b) and (c) show the speed and the altitude profiles, respectively. The throttle control input is shown in Fig. 24 (d). Figs. 24 (e), and (f) show the deflection of the control surfaces, where the aileron surface deflects to follow the commanded turning rate. The pitch, roll and yaw rates are shown in Figs. 24 (g),(h), and (i), respectively. The proposed strategy navigates the UAV safely for all the initial heading angles from 48° and 149°. Results highlight the advantage of the proposed strategy and its viability in practical application.

VII.   Conclusions

A new guidance strategy for navigation through urban canyons is proposed for UAVs with a single forward facing camera. The strategy considers focus of expansion for the partition the image and generates a turn rate which is inversely proportional to the optical flow difference on the two sides of the image. The proposed strategy overcomes the limitations of the existing balance strategy while the UAV directly faces a wall or an obstacle. Analytical comparison of the proposed strategy with the balance strategy is carried out to highlight the superior obstacle avoidance behavior of the proposed strategy. Simulations are carried out using point mass UAV model for straight, L, and T shaped urban canyons, and their combinations created in the virtual reality toolbox VRML in MATLAB® with a real image. Simulation studies with 6 DoF model of Zagi MAV are presented, showing the realistic viability of the proposed method. Simulation results highlight that the proposed strategy guides the UAV through complex realistic scenarios overcoming a big limitation of the balance strategy. Moreover, the strategy works well for straight canyons with a wider range of initial heading angles as compared to the balance strategy. Limitations of the method include a jitter introduced in the guidance command while having a low optical flow difference. Additionally, center of camera frame can be considered as a computationally feasible alternate to the present focus of expansion based partition of the image in case of negligible side slips and course optical flows.

References

[1]L. Muratet, L. S. Doncieux and J. A. Meyer: A Biometric Navigation System Using Optical Flow for a Rotary-Wing UAV in Urban Environment, *In Int'l Conference on Robotics and Automation*, New Orleans, 2004, pp. 2347–2352.

[2]J. Lwowski, L. Sun, R. M. Saavedra, R. Sharma and D. Pack: A Reactive Bearing Angle Only Obstacle Avoidance Technique for Unmanned Ground Vehicles, *Journal of Automation and Control Research (JACR)*, Vol. 1, 2014, pp. 31–37. doi: 10.11159/jacr.2014.004

[3]K. Souhila and A. Karim: Optical Flow Based Robot Obstacle Avoidance, *Int. Journal of Advanced Robotic Systems*, Vol. 4, No. 1, 2007, pp. 13–16. doi: 10.5772/5715

[4]K. T. Song and J. H. Huang: Fast Optical Flow Estimation and Its Application to Real-Time

Obstacle Avoidance, *In Proceedings of IEEE Int'l Conference on Robotics and Automation (ICRA)*, Seoul, Korea, 2001, pp. 2891–2896. doi: 10.1109/ROBOT

[5]A. Dippold, L. Ma and N. Hovakimyan: Vision-Based Obstacle Avoidance of Wheeled Robots Using Fast Estimation, *Journal of Guidance, Control, and Dynamics*, Vol. 32, No. 6, 2009, pp. 1931–1937. doi: 10.2514/1.46016.

[6]C. Suliman, F. Moldoveanu and M. Cernat: Autonomous Mobile Robot Navigation Using Optical Flow, 6th *Int'l Conference on Interdisciplinarity in Education*, Safranbolu, Turkey, 2011, pp. 312–318.

[7]D. W. Yoo, D. Y. Won and M. J. Tahk: Optical Flow Based Collision Avoidance of Multi-Rotor UAVs in Urban Environments, *Int'l Journal of Aeronautical and Space Sciences*, Vol. 12, 2011, pp. 252–259. doi: 10.5139/IJASS.2011.12.3.252

[8]W. E. Green, P. Y. Oh and G. Barrows: Flying Insect Inspired Vision for Autonomous Aerial Robot Maneuvers in Near-Earth Environments, *IEEE Int'l Conference on Robotics and Automation (ICRA)*, New Orleans, LA, 2004, pp. 2347–2352.

[9]A. Eresen, N. Imamoglu and M. Efe: Autonomous Quadrotor Flight with Vision-Based Obstacle Avoidance in Virtual Environment, *Expert Systems with Applications*, Vol. 39, No. 1, 2012, pp. 894–905. doi./10.1016/j.eswa.2011.07.087

[10]A. R. Roderick, J. J. Kehoe and R. Lind: Vision-Based Navigation Using Multi-Rate Feedback from Optic Flow and Scene Reconstruction, *In Proceeding of the AIAA Guidance, Navigation, and Control Conference*, San Francisco, California, 2005, pp. 1–15.

[11]K. R. Prashanth, P. Shankpal, B. Nagaraja, G. R. Kadambi and S. R. Shankapal: Real Time Obstacle Avoidance and Navigation of a Quad-Rotor MAV Using Optical Flow Algorithms, *SASTECH Journal*, Vol. 12, No. 1, 2013, pp. 31–35.

[12]K. Schauwecker, N. R. Ke, S. A. Scherer and A. Zell: Markerless Visual Control of a Quad-Rotor Micro Aerial Vehicle by Means of On-Board Stereo Processing, *Autonomous Mobile Systems*, 2012, pp. 11–20. doi: 10.1007/978-3-642-32217

[13]S. Hrabar, G. S. Sukhatme, P. Corke, K. Usher and J. Roberts: Combined Optic-Flow and Stereo-Based Navigation of Urban Canyons for a UAV, *In Proceedings of the IEEE/RSJ Int'l Conference on Intelligent Robots and Systems*, Edmonton, Alberta, Canada, 2005, pp. 3309–3316.

[14]H. Choi, Y. Kim and I. Hwang: Reactive Collision Avoidance of Unmanned Aerial Vehicles Using a Single Vision Sensor, *Journal of Guidance, Control, and Dynamics*, Vol. 36, No. 4, 2013, pp. 1234–1240. doi: 10.2514/1.57131.

[15]B. Call, R. Beard, C. Taylor and B. Barber: Obstacle Avoidance for Unmanned Vehicles Using Image Feature Tracking, *AIAA Guidance, Navigation, and Control Conference and Exhibit*, Keystone, Colorado, 2006, pp. 3406–3414.

[16]C. Schlaile, O. Meister, N. Frietsch, C. Keler, J. Wendel and G. F. Trommer: Using Natural Features for Vision Based Navigation of an Indoor-VTOL MAV, *Aerospace Science and Technology*, Vol. 13, 2009, pp. 349–357. doi:10.1016/j.ast.2009.09.001

[17]M. Tistarelli, E. Grosso and G. Sandini: Dynamic Stereo in Visual Navigation, *IEEE Conference on Cumpter Vision and Pattern Recognition*, Lahaina, Hawaii, 1991, pp. 186–193.

[18]P. O'Donovan: Optical Flow: Techniques and Applications, *The University of Saskatchewan*, 2005.

[19]P. Getreuer, Linear Methods for Image Interpolation, *Image Processing On Line, Vol. 1, 2011, pp. 1–22.*

[20]*D. Han: Comparison of Commonly Used Image Interpolation Methods, Proceedings of the 2nd International Conference on Computer Science and Electronics Engineering, 2013, pp. 1556–1559.*

[21]*A. L. Gorbunov: Stereoscopic Augmented Reality in Visual Interface for Flight Control, Aerospace Science and Technology, Vol. 38, 2014, pp. 116–123. doi:10.1016/j.ast.2014.08.002*

[22] M. V. Srinivasan, S. W. Zhang, S. W. Lehrer and T. S. Collett, *Honeybee Navigation en Route to the Goal: Visual Flight Control and Odometry*, Journal of Experimental Biology, Vol. 199, 1996, pp. 237–244. doi:10.1.1.115.9306

[23] G. L. Barrows, J. S. Chahl and Y. V. Srinivasan, *Biomimetic Visual Sensing and Flight Control*, In Proceedings 17th Int'l Unmanned Air Vehicle Systems Conference, Bristol, UK, 2002, pp. 159–168.

[24] S. Hrabar and G. Sukhatme: *Vision-Based Navigation Through Urban Canyons*, Journal of Field Robotics, Vol. 26, No. 5, 2009, pp. 431–452. doi: 10.1002/rob.20284

[25] J.L. Barron, D.J. Fleet and S.S. Beauchemin: *Performance of Optical Flow Techniques*, Int'l Journal Computer Vision, Vol. 12, No. 1,1994, pp. 43-77. doi: 10.1007/BF01420984

[26] B.K.P. Horn and B.G. Schunck: *Robust Optical Flow Computation*, Artificial Intelligence, Vol. 17, No. (1-3), 1981, pp. 185–203. doi:10.1016/0004-3702(81)90024-2.

[27] B.D. Lucas and T. Kanade: *An Iterative Image Registration Technique with an Application to Stereo Vision*, In Proceedings of the 7th Int'l Joint Conference on Artificial Intelligence (IJCAI), Vancouver, British, Columbia, 1981, pp. 674–679.

[28] D.J. Fleet and A.D. Jepson: *Computation of component image velocity from local phase information*, IJCV, Vol. 5, No. 1, 1990, pp. 77–104.

[29] P. Anandan: *A Computational Framework and an Algorithm for the Measurement of Visual Motion*, Int. Journal of Computer Vision, Vol. 2, No. 3, 1989, pp. 283–310. doi:10.1007/BF00158167

[30] D.Coombs, M. Herman, T.H. Hong and M.Nashman: *Real-Time Obstacle Avoidance Using Central Flow Divergence, and Peripheral Flown*, IEEE Transactions on Robotics and Automation, Vol. 14, No. 1, 1998, pp. 49–59. doi:10.1.1.63.286

[31] D.K. Liyanage and M.U.S. Perera: *Optical Flow based Obstacle Avoidance for the Visually Impaired*, IEEE Business Engineering and Industrial Applications Colloquium, Kuala Lumpur, Malaysia, 2012, pp. 284–289.

[32] L. Muratet, S. Doncieux, Y. Briere and J.A. Meyer: *A Contribution to Vision-Based Autonomous Helicopter Flight in Urban Environments*, Robotics and Autonomous Systems, Vol. 5, No. 1, 2012, pp. 23–33. doi: 10.1016/j.robot.2004.09.017

[33] S. Suryanarayana, B.L. Deekshatulu, K.L. Kishore and Y.R. Kumar: *Estimation and Removal of Gaussian Noise in Digital Images*, International Journal of Electronics and Communication Engineering, Vol. 50, No. 4, 2005, pp. 195–209.

[34] R. W. Beard and T. W. McLain: *Navigation, Guidance, and Control of Small Unmanned Aircraft*, Princeton University Press, Princeton, NJ, USA, 2012.